Fast and Durable Intraoperative Near-infrared Imaging of Ovarian Cancer Using Ultrabright Squaraine Fluorophores

Takeshi Fukuda, Shinya Yokomizo, Stefanie Casa, Hailey Monaco, Sophia Manganiello, Haoran Wang, Xiangmin Lv, Amy Daniel Ulumben, Chengeng Yang, Min-Woong Kang, Kazumasa Inoue, Masahiro Fukushi, Toshiyuki Sumi, Cheng Wang, Homan Kang, Kai Bao, Maged Henary, Satoshi Kashiwagi, Hak Soo Choi

Highlights	◇卵巣がん治療では、未だに術者の眼と手によってがん組織を識別するため取り残す可能性がある。 ◇手術前に血管内に投与することで手術中に小さいがんでもはっきりと見える蛍光試薬を開発。
概要	共同研究チームは、近赤外線レーザーを照射することで卵巣がん細胞を手術中に可視化する新しい蛍光色素を開発しました。本成果は、2022 年 2 月 23 日（ドイツ時間）にドイツ化学会誌である「Angewandte Chemie」誌に掲載されました。卵巣がん治療において手術で病巣を完全に切除することは、治療成績を向上させるための最も重要な因子です。 近年、がんや組織をはっきりと標識することができる蛍光ガイド手術は、腫瘍の局在を明らかにすることで取り残しを減らし、外科的な腫瘍切除成績を向上させる技術として注目を集めています。今回本研究グループは、近赤外領域に蛍光を持つスクアライン色素の化学構造や電荷に修飾を加えることで、高輝度で安定した卵巣がん指向性のある蛍光色素 OCTL14 の開発に成功しました。OCTL14 を卵巣がん腹膜播種マウスモデルに投与したところ、投与 24 時間後まで 1 ミリ以下の微小な腫瘍組織を検出し、その蛍光ガイド下での手術では肉眼だけに比べて多数の腫瘍の除去が可能でした。OCTL14 は低分子蛍光色素分子であり、比較的簡単、安価に大量合成も可能であり広い臨床応用にも適しています。 この蛍光物質が将来的に認可され、手術に応用されると、産婦人科医による卵巣がんの手術成績を向上させ、女性患者の予後を改善する画期的な新技術となることが期待されます。 ‘卵巣がん完全切除に向けた新たなナビゲーター！小さながんでもはっきり見える蛍光試薬を開発’. 大阪市立大学. https://www.osaka-cu.ac.jp/ja/news/2021/220329. (参照 2022-03-29)
資金・特許等について	本研究は、ハーバード大学医学部／マサチューセッツ総合病院の計画研究の一部として行われました。 ・ 米国立衛生研究所(R01EB022230)「Image-Guided Drug Delivery for Pancreatic Neuroendocrine Tumor」 ・ 米国立衛生研究所(R01HL143020)「Nanochelation Therapies for Iron Overload Disorders」 報告された蛍光物質は、研究を主導したハーバード大学医学部／マサチューセッツ総合病院、化学合成を主導したジョージア州立大学により特許出願されております。

Fast and Durable Intraoperative Near-infrared Imaging of Ovarian Cancer Using Ultrabright Squaraine Fluorophores

Takeshi Fukuda[a], [b], Shinya Yokomizo[a], [c], Stefanie Casa[d], Hailey Monaco[a], Sophia Manganiello[a], Haoran Wang[a], Xiangmin Lv[e], Amy Daniel Ulumben[a], Chengeng Yang[a], Min-Woong Kang[a], [f], Kazumasa Inoue[c], Masahiro Fukushi[c], Toshiyuki Sumi[b], Cheng Wang[e], Homan Kang[a], Kai Bao[a], Maged Henary[d], [g]*, Satoshi Kashiwagi[a]* and Hak Soo Choi[a]*

[a] Dr. T. Fukuda, S. Yokomizo, H. Monaco, S. Manganiello, H. Wang, A. D. Ulumben, C. Yang, Prof. M. W. Kang, Dr. H. Kang, Dr. K. Bao, Prof. S. Kashiwagi, Prof. H. S. Choi Gordon Center for Medical Imaging, Department of Radiology, Massachusetts General Hospital and Harvard Medical School, Boston, MA 02114, USA. E-mail: hchoi12@mgh.harvard.edu, skashiwagi@ mgh.harvard.edu
[b] Dr. T. Fukuda, Prof. T. Sumi
Department of Obstetrics and Gynecology, Osaka City University Graduate School of Medicine, 1-4-3, Asahimachi, Abeno-ku, Osaka, 545-8585, Japan
[c] S. Yokomizo, Prof. K. Inoue, Prof. M. Fukushi
Department of Radiological Sciences, Tokyo Metropolitan University, 7-2-10 Higashi-Ogu, Arakawa, Tokyo 116-8551, Japan
[d] S. Casa, Prof. M. Henary
Department of Chemistry, Georgia State University, Atlanta, GA 30303, USA
Email: mhenary1@gsu.edu
[e] Dr. X. Lv, Prof. C. Wang
Vincent Center for Reproductive Biology, Vincent Department of Obstetrics and Gynecology, Massachusetts General Hospital, Boston, MA 02114, USA
[f] Prof. M. W. Kang
Department of Thoracic and Cardiovascular Surgery, School of Medicine, Chungnam National University, Daejeon 301-721, South Korea
[g] Prof. M. Henary
Center for Diagnostics and Therapeutics, 145 Piedmont Avenue S.E., Atlanta, GA 30303, USA

Supporting information for this article is given via a link at the end of the document.

Abstract: The residual tumor after surgery is the most significant prognostic factor of patients with epithelial ovarian cancer. Near-infrared (NIR) fluorescence-guided surgery is actively utilized for tumor localization and complete resection during surgery. However, currently available contrast-enhancing agents display low on-target binding, unfavorable pharmacokinetics, and toxicity, thus not ideal for clinical use. Here we report ultrabright and stable squaraine fluorophores with optimal pharmacokinetics by introducing an asymmetric molecular conformation and surface charges for rapid transporter-mediated cellular uptake. Among the tested, OCTL14 shows low serum binding and rapid distribution into cancer tissue *via* organic cation transporters (OCTs). Additionally, the charged squaraine fluorophores are retained in lysosomes, providing durable intraoperative imaging in a preclinical murine model of ovarian cancer up to 24 h post-injection. OCTL14 represents a significant departure from the current bioconjugation approach of using a non-targeted fluorophore and would provide surgeons with an indispensable tool to achieve optimal resection.

Introduction

The standard treatment for the most common epithelial ovarian cancer is surgery followed by chemotherapy [1]. One of the significant prognostic factors of ovarian cancer patients is the amount of residual tumor after surgery [2]. Therefore, it is crucial to reduce the tumor burden during surgery as much as possible. However, accurate detection, localization, and differentiation of peritoneally-disseminated ovarian cancer from normal tissue are often challenging, which currently relies on visual inspection and palpation [3]. To overcome these limitations, fluorescence-guided surgery (FGS) has emerged as a technique to highlight cancer cells and provide surgeons with real-time image guidance [4]. FGS has been approved for various procedures, including identification of tumor margin, sentinel lymph node mapping, angiography, and lymphography [5], and improved tumor resection rates and prognosis while minimizing normal tissue damage [6]. In response to this, a number of new imaging methods for FGS have been developed [4c]. Amongst these, near-infrared (NIR) imaging features reduced scattering, minimal tissue absorption with high tissue penetration depth, low tissue autofluorescence interference [7], and is better suited for FGS offering high signal-to-background ratio (SBR) and resolution for imaging of deep tissue [8].

For FGS of cancer, various tumor-targeting molecules, such as antibodies, nanoparticles, proteins, peptides, and small molecules, have been developed [4c, 9]. However, multifunctional nanoparticles showed the unexpected accumulation in vital organs, and their unknown long-term toxicity raises safety concerns [10]. Antibodies targeting tumor biomarkers are generally too large to transfer into tumor tissues and show slow clearance, resulting in a low target-to-background ratio (TBR) [11] and prolonged waiting time after administration [10, 12]. Alternatively, small molecules measuring 10–1000-fold smaller than peptides and proteins, which can rapidly readily diffuse into and accumulate in target tissues and then be rapidly excreted from the system [13], have been explored to achieve a high TBR [8b]. One of such strategies is the use of a ligand for the folate receptor α (FRα), which is overexpressed in ovarian cancer [14]. A recent phase II clinical study evaluated a folate analog conjugated to a NIR fluorescent fluorophore known as OTL38 with promising results [14c]. However, a relatively high false-positive rate of 23% was reported because of its off-target binding to FRβ. In addition, it still needs a prolonged clearance time after intravenous injection ranging from 2 to 18 h prior to surgery [14a, 14c]. Currently, an FDA-approved small molecule NIR probe indocyanine green (ICG) is available in the clinic; however,

it shows no specific targeting capability [15] and has significant limitations in FGS of cancer [16]. Contrary, a "structure-inherent targeting (SIT)" strategy has been utilized to improve the biodistribution and targetability of molecular probes by tuning the lipophilicity and charge of backbone structures, allowing for high uptake in specific tissues with low non-specific binding [17]. In this study, new squaraine chromophores are developed for fast and efficient targeting of ovarian cancers and their FGS. These zwitterionic and planar structured squaraines are water-soluble and stable in aqueous solutions due to the molecule's 3D conformation in which the core is protected, resulting in reduced serum binding and superb optical properties in the NIR wavelengths [18], allowing surgeons to more precisely perform surgical tumor resection.

Results and Discussion

To achieve rapid and durable intraoperative imaging of ovarian cancer, a series of asymmetric squaraine fluorophores were designed and synthesized (**Fig. 1a**). Historically, squaraines showed instability owing to their highly chemically- and photolytically-labile oxocyclobutenolate ring, significantly limiting their applications. Recently, a robust solution to the stability issues was developed by synthesizing an intramolecular salt bridge to protect the central oxocyclobutenolate ring of the squaraine fluorophore with a quaternary ammonium cation which increased the molar absorptivity and quantum yield in serum due to the enhanced rigidity associated with its locked structure [19]. The most crucial modification made to the compounds is the introduction of halogens: fluorine, chlorine, and bromine, resulting in increased molar absorptivity and bathochromic shifts associated with shielding of inner electrons and high electronegativity [20]. Although the introduction of the quaternary ammonium was largely for the salt-bridge, this moiety also increases the solubility of contrast agents, making them better suited for biological applications [19]. In this work, both symmetrical and asymmetrical squaraines were tested for ovarian tissue-specific targeting, and only asymmetrical squaraines showed relatively high uptake in the ovary. Interestingly, asymmetric squaraines are better suited for further modifications of the scaffold without significantly affecting the stability. In response to this, we focused on testing asymmetrical squaraines in the current study. **Figure S1** outlines the formation of the relevant heterocycles, **1-5**, with corresponding substituted phenylhydrazine and 3-methyl-2-butanone under acidic conditions [4b, 4c, 7b]. The following step was to alkylate compounds **1-5** with (3-bromopropyl) trimethylammonium bromide (BrTMAB) under reflux in acetonitrile (ACN) to afford the final 3-H indolium salt derivatives **6-10** [4b, 4c, 7b]. After the synthesis of salts **6-10**, a squaric acid with isopropoxy protecting groups was allowed to react with 1,2,3,3-tetramethyl-3*H*-indolium iodide salt under basic conditions yielding the desired semi-squaraine **11** [21]. Compound **11** and the corresponding salts **6-10** were reacted in butanol and benzene mixtures containing quinoline as a base and heated under reflux using a Dean-Stark apparatus to furnish the asymmetric squaraine dyes **12-16** [19]. ^{1}H NMR, ^{13}C NMR, and HRMS of compound **13** are shown in **Figure S2-S4**. The novel squaraine fluorophore is less than 600 Da and can be synthesized reproducibly.

Next, physicochemical and optical properties of the squaraine fluorophores were determined (**Fig. 1b**).

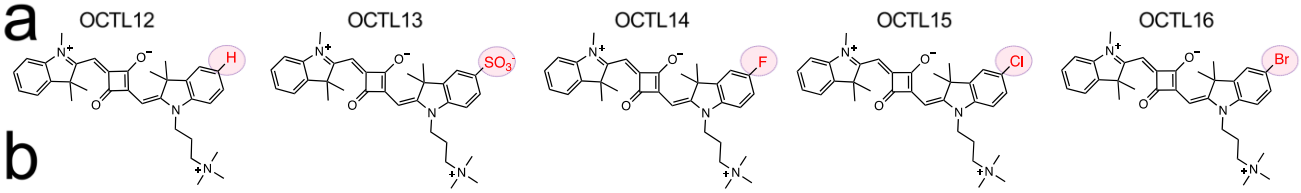

b

OCTL	MW (g/mol)	LogD (pH=7.4)	TPSA (Å²)	HBD	HBA	Charges (+/-)	Strongest basic pKa	Strongest acid pKa	Plasma (%Bound)	Ext. Coeff. ($M^{-1}cm^{-1}$)	QY (%)	Abs. Max (nm)	Fl. Max (nm)
OCTL12	510.31	-1.09	46.38	0	3	+2/-1	1.29	6.85	2.76	191,800	57.00	635	652
OCTL13	589.26	-1.46	103.58	0	6	+2/-2	0.11	-3.67	4.42	99,800	65.07	636	650
OCTL14	528.3	-0.91	46.38	0	3	+2/-1	0.81	6.6	4.46	106,400	79.56	635	649
OCTL15	544.27	-0.45	46.38	0	3	+2/-1	0.63	6.59	47.87	99,600	80.61	637	650
OCTL16	588.22	-0.28	46.38	0	3	+2/-1	0.86	6.56	68.32	110,600	75.91	637	657

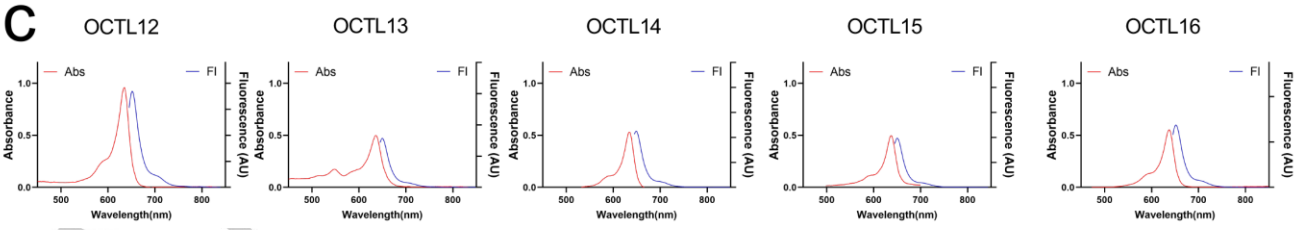

Figure 1. Chemical structures, physicochemical properties, and optical properties of the functionalized squaraines. (a) Chemical structures of the five asymmetric squaraine derivatives. (b) Quantitative calculation of physicochemical properties of the squaraine fluorophores. (c) Optical properties of the squaraine fluorophores in phosphate-buffered saline (PBS, pH 7.4) with 5% bovine serum albumin (BSA). MW, molecular weight; TPSA, topological polar surface area; HBD, hydrogen bond donors; HBA, hydrogen bond acceptors; Ext. Coeff., extinction coefficient; QY, quantum yield; Abs, absorbance; Fl, fluorescence.

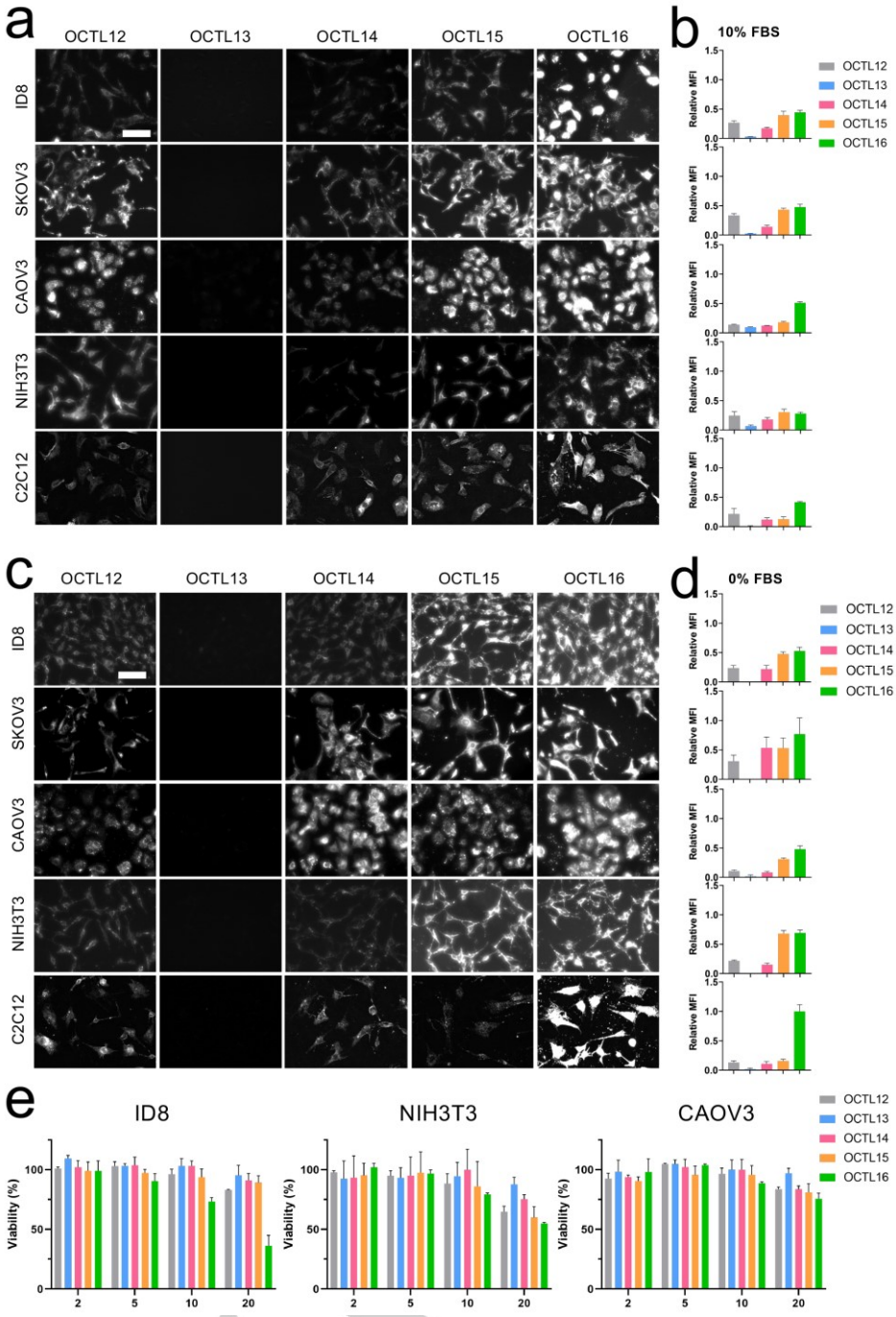

Figure 2. Tumor cell targetability and cytotoxicity of squaraines. Murine and human ovarian cancer cell lines including ID8 cells, CAOV3 and SKOV3 cells, NIH3T3 fibroblast, and C2C12 muscle cells were cultured and incubated at 37°C for 30 min in 10% or 0% FBS media in the presence of 2 μM of OCTL12, OCTL13, OCTL14, OCTL15, and OCTL16 and imaged using an epifluorescence microscope. (a-d) Representative fluorescence images of cells in (a) 10% or (c) 0% FBS media. Scale bar = 100 μm. Quantitative measurements of the fluorescence intensity of cells in (b) 10% and (d) 0% FBS. The relative mean fluorescence intensity (MFI) of cells in each group was calculated by comparing the highest OCTL16 group of C2C12 cells in the presence of serum. *P < 0.05 by one-way ANOVA followed by Tukey's multiple comparisons test (n = 3, mean ± s.e.m.). (e) Cytotoxicity of squaraines. Cells were treated with 2, 5, 10, and 20 μM of each compound for 24 h, followed by an assessment of cell viability using the Cell Counting Kit-8 (CCK-8). *P < 0.05 by two-way ANOVA followed by Tukey's multiple comparisons test (n = 3, mean ± s.e.m.).

OCTL13, which has a sulfonate on the phenyl ring, showed the highest hydrophilicity (LogD at pH 7.4 = -1.46), while OCTL16 with a bromine atom demonstrated increased lipophilicity (LogD at pH 7.4 = -0.28). The TPSA values for OCTL12 with no substituent on the phenyl ring, OCTL14 with a fluorine atom, OCTL15 with a chlorine atom, and OCTL16 with a bromine atom were similar with a total charge of +1; the TPSA value for the sulfonate containing OCTL13 was higher than that of the others with a net charge of zero. All fluorophores consistently showed NIR fluorescence with the excitation and emission maxima at 635-637 nm and 649-657 nm, respectively, compatible with the 700-nm NIR fluorescence channel of the FLARE imaging system (**Fig. 1c**). All squaraines show exceptional optical properties for intraoperative imaging with a high molar absorptivity of 99,600-191,800 $M^{-1}cm^{-1}$ and quantum yield (QY) of 57-80%, respectively, representing ultrahigh brightness (**Fig. 1b**, **Fig. S5a**). Consistent with our previous report [19], all the tested squaraines were photostable in serum, but not in PBS (**Fig. S5b**).

The ovarian cancer cell targetability of each squaraine fluorophore was examined *in vitro* by fluorescence microscopy using murine ID8, human CAOV3, and SKOV3 ovarian cancer cells, with NIH3T3 fibroblasts and C2C12 myoblasts used as controls. OCTL12, OCTL14, OCTL15, and OCTL16 showed accumulation in ovarian cancer cells in the presence (**Fig. 2a,b**) or absence (**Fig. 2c,d**) of serum. OCTL13 with the highest hydrophilicity showed less accumulation in all cell lines regardless of serum presence. Halogenated (OCTL14, OCTL15, and OCTL16) and non-halogenated (OCTL12) squaraines were taken up by both murine and human ovarian cancer cells in similar magnitudes compared to normal cells, and the uptake was not significantly affected by the presence of serum (**Fig. 2a-d**) which indicates a minimal role of albumin or lipoprotein in cellular uptake.

Although we did not observe a notable difference in cellular uptake of squaraines between cancer and normal cell lines in this experimental model, the relative uptake of OCTL14 and OCTL15 by C2C12 cells was smaller compared to that by other cells (**Fig. 2a-d**). This uptake pattern was not significantly affected by the presence of serum. In addition, C2C12 cells showed relatively higher uptake of OCTL16 in the presence of serum (**Fig. 2a-d**). On the other hand, NIH3T3 cells showed relatively high uptake of OCTL15 and OCTL16 in the presence of serum (**Fig. 2a-d**). These results suggest the presence of distinct uptake mechanisms of squaraines in NIH3T3 and C2C12 cells from cancer cells. It was next determined if squaraine fluorophores display any toxicity to cells *in vitro*. To this end, murine ID8 and human CAOV3 ovarian cancer cells as well as NIH3T3 fibroblasts were incubated with various concentrations of squaraine fluorophores and then evaluated for cell viability (**Fig. 2e**). In ID8 and NIH3T3 cells, OCTL16 with bromine showed significant toxicity at a high concentration beyond 10 μM. Hydrophobic OCTL12 and OCTL15 showed modest toxicity at 20 μM, but OCTL13 and OCTL14 displayed almost no toxicity up to 10-20 μM. In CAOV3 cells, all compounds showed little toxicity at the tested concentrations up to 20 μM. These results indicate that squaraine fluorophores especially OCTL13 and 14 can be used safely for bioimaging and image-guided cancer surgery. To determine the *in vivo* biodistribution of squaraines, 100 nmol of each fluorophore was administered to mice followed by intravital NIR imaging and *ex vivo* tissue biodistribution 6 h after injection under the FLARE imaging system. The +1 charged OCTL14, OCTL12, OCTL15, and OCTL16 (log*D* = **−** 1.09 to **−** 0.28) showed relatively high SBR in the duodenum or intestine in addition to the kidneys (**Fig. S6a**), indicating excretion through the hepatobiliary route. OCTL14 and OCTL15 (log*D* = **−** 0.91 to **−** 0.45) were found in the bladder (**Fig. S6a**). The noncharged, hydrophilic OCTL13 (log*D* = **−** 1.46) showed a relatively high SBR in the duodenum or intestine but lower signals in the kidneys compared to the other compounds (**Fig. S6b**), indicating that this fluorophore clears from the body mainly through the hepatobiliary excretion routes.

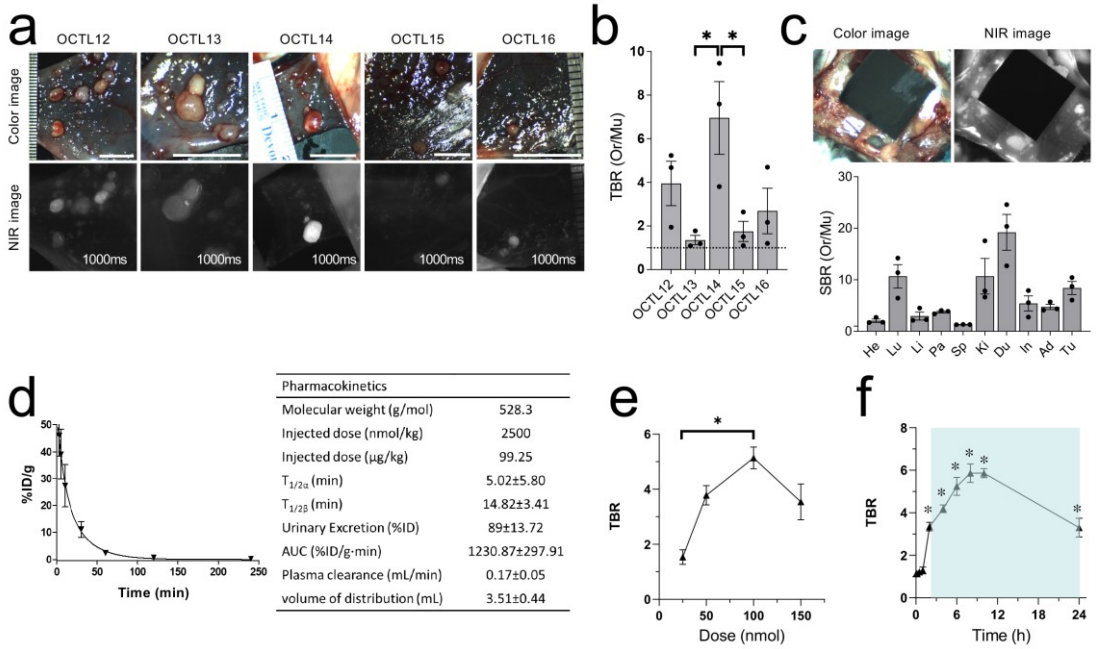

Figure 3. *In vivo* evaluation of tumor cell targetability of squaraines in a mouse model of ovarian cancer. (a) Mice were injected with 100 nmol of each squaraine fluorophore 6 h prior to imaging. Scale bars = 5 mm. (b) Quantitative analysis of target-to-background ratio (TBR) of peritoneal tumors for each squaraine fluorophore (n = 3, mean ± s.e.m.). *P < 0.05 by one-way ANOVA followed by Tukey's multiple comparisons test. (c) Tumor targetability and biodistribution of OCTL14. Intestine and liver were covered with black paper to block fluorescent signals from these organs. The graph shows the SBR of resected organs and tumors. Scale bar = 1 cm. (d) Pharmacokinetics of OCTL14. 100 nmol of OCTL14 was injected intravenously into CD-1 mice. Blood concentration (%ID/g) decay curve and distribution ($t_{1/2\alpha}$) and elimination half-life ($t_{1/2\beta}$) values are shown (n = 3, mean ± s.e.m.). Urine samples were collected 4 h post-injection. %ID/g, percent injected dose per gram; AUC, the area under the curve. (e) Dose-response curve of OCTL14. Tumor-bearing mice were intravenously injected with 25, 50, 100, and 150 nmol of OCTL14. TBR was determined for tumor 6 h post-injection by NIR imaging. (f) Quantitative time-course assessment of TBR. Tumor-bearing mice were intravenously injected with 100 nmol of OCTL14. TBR was observed at 3, 10, 30, 60, 120, 240, 360, 480, and 600 min and 24 h post-injection by NIR imaging (n = 3, mean ± s.e.m.). The blue window shows the duration in which significantly higher TBR was obtained compared to that at 3 min. *P < 0.05 by one-way ANOVA followed by Tukey's multiple comparisons test.

Histological evaluation consistently revealed that OCTL14 and OCTL15 distributed in both the renal cortex and medulla, suggesting renal clearance, while OCTL12 and OCTL16 accumulated predominantly in the medulla (**Fig. S6c**), indicating little renal clearance, if any. Diffuse distribution in hepatocytes was observed for all squaraine fluorophores, indicating hepatobiliary excretion (**Fig. S6c**). Next, the targetability of the squaraines to ovarian cancer was examined in a murine model of ovarian cancer. In this model, many metastatic peritoneal tumors ranging in size from < 1 mm to 5 mm were observed throughout the abdominal cavity. First, 100 nmol of each squaraine fluorophore was administered to tumor-bearing mice followed by intravital NIR imaging and *ex vivo* tissue biodistribution 6 h after injection. NIR imaging demonstrated that all squaraines accumulated in the tumor with various degrees of TBR (**Fig. 3a**). The TBR of OCTL14 was significantly higher than that of OCTL13 and OCTL15 ($P < 0.05$) and marginally higher than those of OCTL12 and OCTL16 (**Fig. 3b**), showing that the strongest signal on the tumors arose from +1 charged OCTL14, which has fluorine on the ring, followed in order by +1 charged OCTL12 without a halogen, +1 charged OCTL16 with bromine, +1 charged OCTL15 with chlorine, and +1/−1 charged OCTL13 without a halogen. NIR imaging showed that OCTL14 accumulated in tumor tissues of all sizes with an ultralow background in the surrounding normal tissue (**Fig. 3c**). Biodistribution studies showed excellent SBR of the tumor ranging from 6:1-10:1 (**Fig. 3c**). OCTL13 with a high TPSA value (103.58 Å^2) showed minimal tumor targeting compared to other fluorophores (46.38 Å^2) *in vitro* (**Fig. 2**) and *in vivo* (**Fig. 3**). Fluorophores with low TPSA values showed variable but notable tumor targeting, which suggests that TPSA is an important factor in determining membrane permeability as well as tumor targetability. These results indicate that hydrophilic molecules with low Log*D* (≈ -1.0), low TPSA (< 50 Å^2), and positive charge (+1) favored accumulation in ovarian cancer. To further analyze the physicochemical properties of the squaraine fluorophores, a plasma protein binding test was performed using the rapid equilibrium dialysis (RED) system. OCTL14, the fluorophore with the highest tumor uptake, showed a low plasma protein-bound fraction (4.5 % bound) (**Fig. 1b**). The second best-performing +1 charged OCTL12 (log*D* = **−**1.09) also had a similarly low bound fraction (2.8 % bound) compared to that of OCTL15 (47.9 % bound, log*D* = **−**0.45) or OCTL16 (68.3% bound, log*D* = **−**0.28) (**Fig. 1b**), which had low tumor uptake (**Fig. 3b**). The least performing OCTL13 also showed low binding (4.4 % bound, log*D* = **−**1.46), but this molecule has net neutral charge. These results suggest that the low binding affinity of positively charged OCTL14 to serum proteins supports its rapid diffusion into tumor tissue without being sequestered by serum proteins, which is consistent with our previous work showing that low plasma binding of small molecule tumor-targeting fluorophores favors tumor targeting [22]. These results are also consistent with the finding that the presence of serum did not alter cellular uptake of OCTL14 in ovarian cancer cells (**Fig. 2a-d**). The pharmacokinetic parameters of OCTL14 were further evaluated after a single intravenous injection. The blood concentration decay curve indicated a two-compartment model with a blood half-life of 14.8 min and an area under the curve (AUC) of 1,231 %ID/g·min (**Fig. 3d**), indicating that OCTL14 displays rapid excretion through bile and urine. The short blood half-life of OCTL14 indicates that molecules that are not bound to the target will be excreted promptly from the body, which decreases circulation time, nonspecific uptake, and potential toxicity.

An optimal dose of OCTL14 for ovarian cancer imaging was determined by intravenous injection of 25, 50, 100, and 150 nmol of OCTL14 followed by measuring the TBR of peritoneal tumor nodules 6 h post-injection. Escalation of the dose up to 100 nmol improved TBR (**Fig. 3e, S7a**). Next, a quantitative time-course assessment of TBR after OCTL14 injection was performed to determine the optimal time window for FGS using the optimized dose of 100 nmol. The TBR reached values greater than 3 at 2 h post-injection and then kept increasing until 8 h post-injection (TBR = 5.86). TBRs between 2 and 24 h after injection were significantly higher than that at 3 min, indicating that a single bolus injection of 100 nmol OCTL14 is able to provide optimal fluorescent signals between 2 and 24 h post-injection (**Fig. 3f, S7b**), indicating that a single bolus injection of OCTL14 allowed surgeons to visualize the tumor location during the entire surgery. Together, OCTL14 is sufficiently retained in tumor tissue for operators to localize tumors with high contrast during ovarian cancer surgery. To determine the excretion route of OCTL14, we performed a time-course intravital imaging and *ex vivo* tissue biodistribution study up to 4 h post-injection under the FLARE imaging system. Strong fluorescence signals were observed in the liver and gallbladder shortly after injection (0.5 h), which decreased notably over time as observed in the thoracic cavity and resected organs (**Fig. S8a**). The SBR of OCTL14 in the resected duodenum and intestines increased over time and reached its peak at 1-2 h post-injection (**Fig. S8b**). These results indicate that OCTL14 initially accumulates in the liver and subsequently clears into the gastrointestinal track. On the other hand, the fluorescence signal was observed in the kidney shortly after injection (0.5 h), which decreased over time as observed in the abdominal cavity and resected organs (**Fig. S8a**). Consistently, the signal in the urinary bladder was relatively weak initially and slowly increased over time (**Fig. S8a**), indicating a contribution of renal clearance. The result is consistent with the biodistribution data shown in **Fig. S6**, proving that the tested squaraine fluorophore clears rapidly through the hepatobiliary excretion route along with slow renal excretion. Histologically, strong fluorescence signals from the three best-performing dyes, OCTL12, OCTL14, and OCTL16, were detected throughout the tumor tissue with no substantial fluorescence signals in surrounding normal tissues (**Fig. S9a**). High-magnification images show accumulation of OCTL14 in the cytoplasm of the tumor cells and relatively homogenous distribution throughout the tumor tissue, indicating that this compound can penetrate deep into tumor tissue *via* diffusion mechanisms and enter cancer cells (**Fig. 4a**), as diffusion is the primary mechanism for tissue delivery of small molecules less than 1,000 Da [13a]. The modestly performing OCTL13 and OCTL15 showed almost no fluorescence signal in tumor tissue, respectively (**Fig. S9a**). Interestingly, OCTL12, OCTL14, OCTL15, and OCTL16 accumulated in granulosa cells in the ovary, and epithelial cells in the fallopian tube, but OCTL13 accumulated in ovarian interstitial cells only (**Fig. S9a**). These results indicate that squaraine fluorophores with optimized physicochemical properties show affinity to ovarian and fallopian tube tissue and can detect cancer originating from ovarian and fallopian tube epithelia.

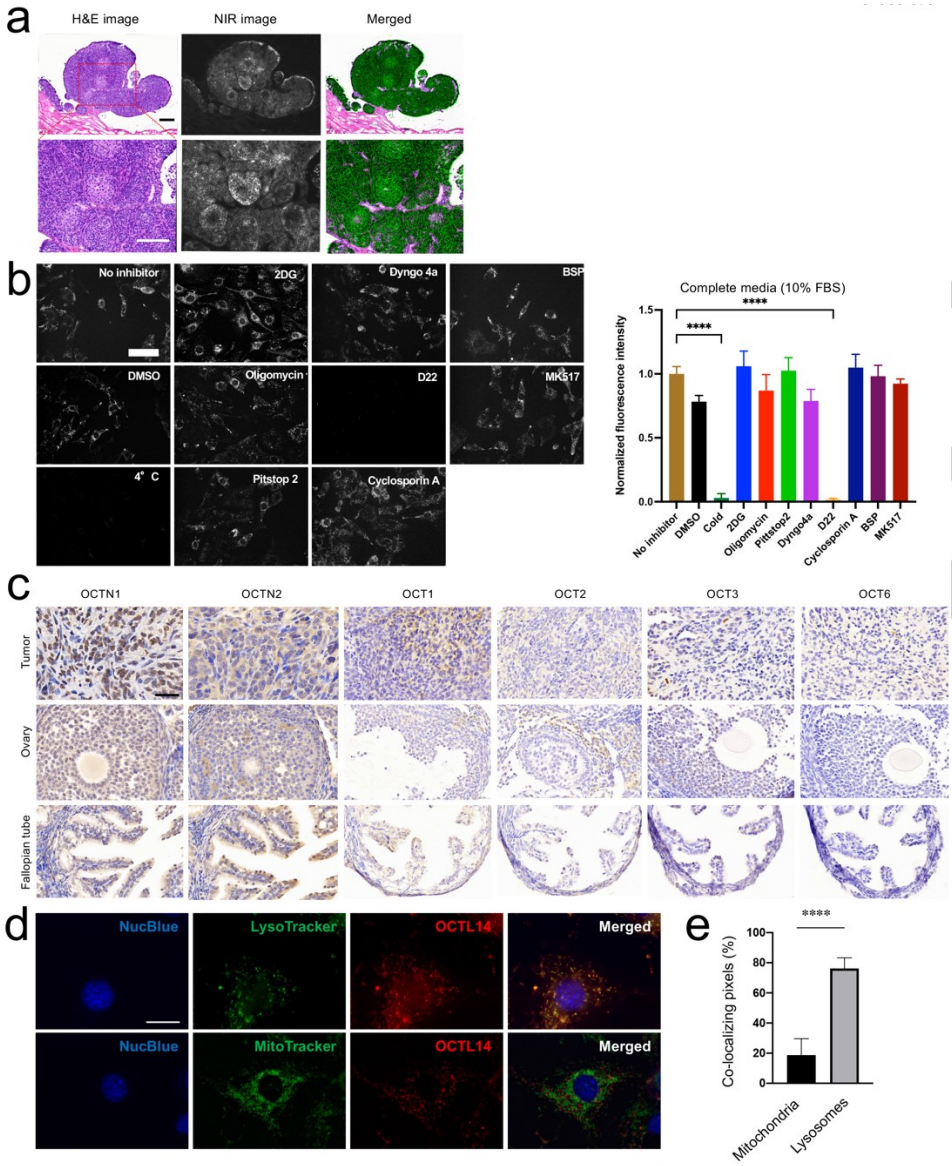

Figure 4. The mechanism of cellular uptake for OCTL14. (a) Histological analysis of OCTL14 injected tumor. Hematoxylin and Eosin (H&E), NIR fluorescence, and merged images of resected tumors are shown. Scale bars = 200 μm. (b) Inhibition assay of cellular uptake of OCTL14 in ID8 cells. Cells were pre-blocked with bromsulphthalein (BSP), cyclosporin A, MK-571, D22, 2DG, oligomycin, Dyngo 4a, Pitstop 2 for 5-30 min or incubated and then incubated with 2 μM of OCTL14 for 30 min. Alternatively, cells were incubated with 2 μM of OCTL14 at 4 °C for 30 min. Scale bar = 100 μm. **P* < 0.05 by one-way ANOVA followed by Tukey's multiple comparisons test (*n* = 3, mean ± s.e.m.). (c) Immunohistochemical analysis of OCTN1, OCTN2, OCT1, OCT2, OCT3, and OCT6 expression in the target tissue. Tumors and adnexa were stained with anti- OCTN1, OCTN2, OCT1, OCT2, OCT3, and OCT6, followed by appropriate secondary antibody using avidin-biotin complex/diaminobenzidine histochemistry. Scale bar = 50 μm. (d) Subcellular localization of OCTL14 (10 μM) in ID8 cells was determined after 30 min of incubation at 37 °C. Nuclei, mitochondria, or lysosomes were stained with NucBlue™, MitoTracker Green FM, or LysoTrackerTM Red DND-99 L7528 and imaged using an epifluorescence microscope. Scale bar = 20 μm. (e) Co-localization index of OCTL14 with MitoTracker Green or LysoTracker Red. The index was calculated by dividing the area of overlap between OCTL14 and MitoTracker or LysoTracker by the total area of MitoTracker or LysoTracker, respectively. The Co-localization index was determined in 6 photographic areas (70 × 92 μm^2 each) for each probe (*n* = 3 ± s.d.). *****P* < 0.0001 by two-tailed Student's t-test.

The OCT family consists of the SLC22 (solute carrier 22) subfamily, which also includes the organic carnitine (zwitterion) transporters (OCTNs), and play critical roles in the regulated transcellular movement of a wide variety of xenobiotics, including the small organic cationic molecules used in this study [23]. Following the results in the cellular uptake and histology study, we hypothesized that OCTL14 was taken up in target tissue *via* OCTs. To this end, ID8 ovarian cancer cells were treated with inhibitors for transporters and cellular energy production. To clarify the role of serum proteins, we also performed this study in the presence and absence of serum. Cellular uptake of OCTL14 significantly decreased when cells were incubated at 4°C (**Fig. 4b**), indicating that OCTL14 hardly enters cells *via* diffusion. Pretreating cells with Dyngo 4a, which is a dynamin-dependent endocytosis inhibitor, or Pitstop 2, which is a clathrin-dependent endocytosis inhibitor, did not result in any appreciable change in cellular uptake (**Fig. 4b**). Similarly, MK-571, which is an inhibitor for ATP-binding cassette (ABC) transporters, induced little change in cellular uptake (**Fig. 4b**). Although tumor-targeting small molecule NIR fluorophores including IR-780 have been shown to enter cells *via* organic anion transporter peptides (OATPs) [24], pretreatment with an OATP inhibitor BSP or cyclosporin A did not result in significant changes in cellular uptake (**Fig. 4b**). Pretreatment with D22, which is an inhibitor of OCTs, induced a significant decrease in cellular uptake (**Fig. 4b**), indicating that OCTL14 cellular uptake was mainly mediated by OCTs. The effect of the cold treatment, endocytosis inhibitors, and transporter inhibitors in the presence of serum (**Fig. 4b**) was not different from that in the absence of serum (**Fig. S9b**), consistently indicating a minimal role of albumin or lipoprotein in cellular uptake of OCTL14.

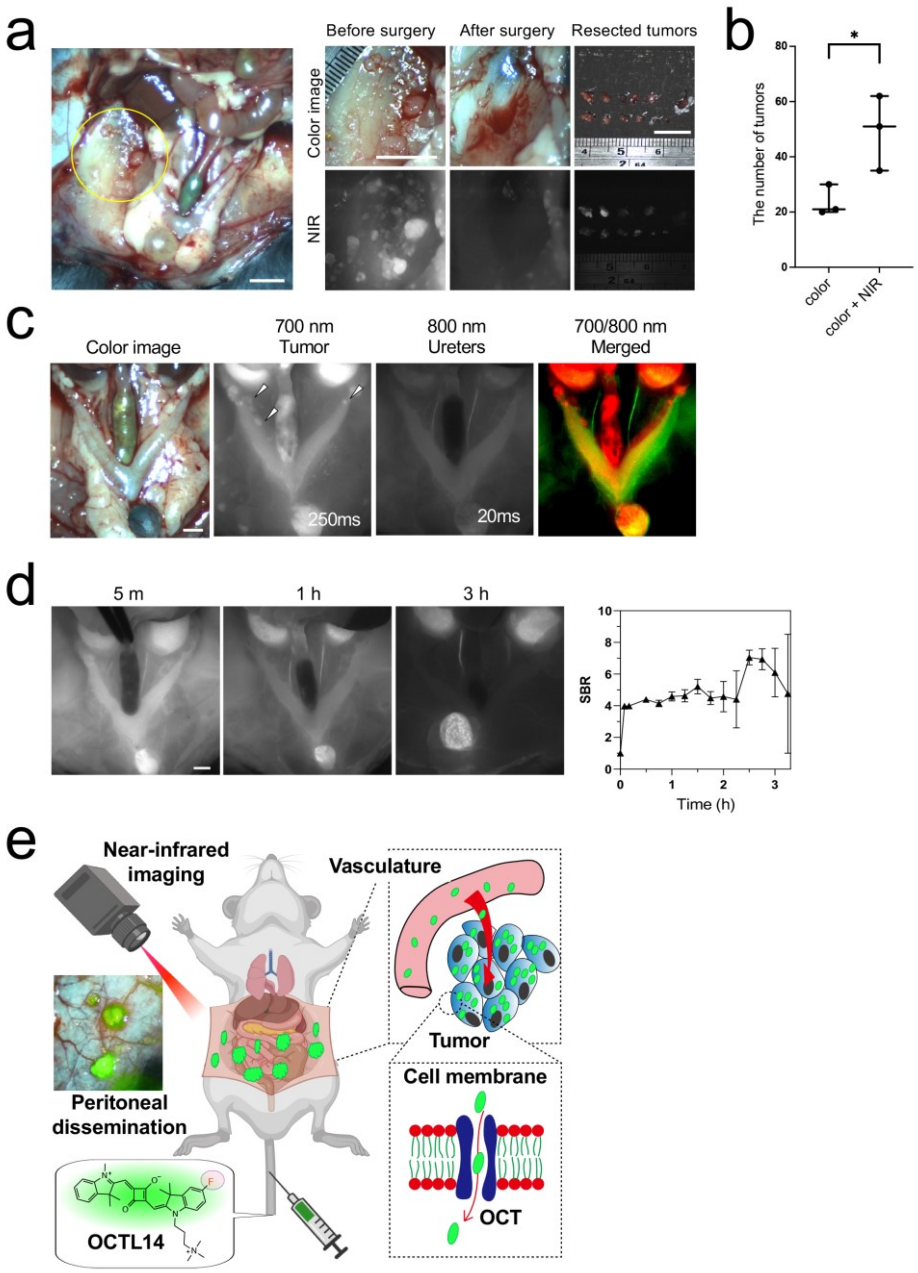

Figure 5. Intraoperative imaging of OCTL14 for FGS. (a) FGS using the squaraine. Tumor-bearing mice were intravenously injected with 100 nmol of OCTL14. FGS was performed 6 h post-injection. The yellow circle indicates the lesions for which intraoperative image-guided surgeries were performed. The middle panels show the tumor locations before/after surgery and resected tumors of different sizes. Scale bars = 1 cm. (b) Clinical impact of the use of OCTL14. The number of tumors detected using color images only was compared to those detected using NIR imaging by experienced surgeons (n = 3, mean ± s.e.m.). *P < 0.05 by two-way ANOVA followed by Tukey's multiple comparisons test. (c) Dual imaging of tumors and ureters. 100 nmol of OCTL14 and 25 nmol of ZW800-PEG were injected intravenously into tumor mice 6 h and 0.5 h prior to imaging, respectively. The 700-nm channel image shows the accumulation of OCTL14 in tumors, while the 800-nm channel image shows the ureteral signals. Arrows indicate the tumor locations. In color–NIR merged image, 700-nm fluorescence (OCTL14) and 800-nm fluorescence (ZW800-PEG) were pseudo-colored red and lime green, respectively, and overlaid onto the color image in real-time. Scale bars = 5 mm. (d) Quantitative time-course assessment of SBR for the ureters (n = 3, mean ± s.e.m.). Scale bar = 5 mm. (e) A summary schematic of the study. A squaraine fluorophore displays ultrabright optical properties and optimal pharmacokinetics, allowing high contrast and durable near-infrared imaging for fluorescence-guided surgery of ovarian cancer. The primary mechanisms of the tumor targetability of OCTL14 involve its rapid diffusion across tumor vasculature and cellular uptake *via* organic cation transporters and retention in the lysosome.

Immunocytochemistry analysis confirmed the expression of OCTN1, OCTN2, OCT1, OCT2, OCT3, and OCT6 in the cytoplasm and plasma membranes of ID8 cells and NIH3T3 cells (**Fig. S10a**). Modulation of the moiety on the phenyl ring can change the characteristics of the squaraines, including hydrophobicity, hydrophilicity, polarity, and electron resonance. OCTL14, which has fluorine on the phenyl ring, exhibited the strong signal in tumors among the derivative fluorophores, whereas OCTL13, which has a sulfonate on the phenyl ring and a +/− 0 electric charge, showed the weak signal in tumors (**Fig. 3a-b**). These results together suggest that charged molecules including OCTL14 are polar, but molecules with one positive charge rendered high affinity to OCTs. The *in vitro* cancer binding tests revealed that OCTL16 was most efficiently taken up by cells, with OCTL13 being the least (**Fig. 2a-d**). OCTL12, OCTL14, and OCTL15 showed almost the same extent of accumulation in cancer cells *in vitro*. However, tumor targetability of compounds is mediated not only by cancer cell uptake but also by plasma pharmacokinetics, which regulates biodistribution throughout the body and excretion routes. Specifically, the signal of OCTL14 was detected in the bladder, suggesting a contribution of renal clearance, but that of OCTL16 was not (**Fig. S6**), indicating that bromine renders unfavorable pharmacokinetics as a contrast-enhancing agent and is thought to be a reason for discrepancies in tumor targetability *in vivo* and *in vitro*. Immunohistochemistry analysis confirmed the expression of OCTN1, OCTN2, OCT1, OCT2, OCT3, and OCT6 in tumors, kidney, liver, and lung (**Fig. 4c, S10b**). OCTN1, OCTN2, OCT1, OCT2, OCT3, and OCT6 expression was seen in the cytoplasm and plasma membranes in ID8 tumor cells (**Fig. 4c**). In the ovary, OCTN1, OCTN2, OCT1, OCT2 and OCT3 were expressed mainly in the cytoplasm and plasma membrane of granulosa cells, which is consistent with the biodistribution of OCTL14 (**Fig. S9a**).

In the fallopian tube, the expression of OCTN1, OCTN2, OCT1 and OCT2 was found mainly in the cytoplasm and plasma membrane of the epithelial cells of the mucosal folds (**Fig. 4c**), which also collaborates the biodistribution of OCTL14 (**Fig. S6a,b**). The expression of OCTN1, OCTN2, OCT1, OCT2, OCT3, and OCT6 in the kidney, liver (hepatocytes), and lung (bronchial and alveolar epithelial cells) was consistent with a previous report [23c] and was co-localized with the biodistribution of OCTL14 in these tissues (**Fig. S6a,b**), confirming the critical role of OCTs/OCTNs in OCTL14 uptake. Recently, ovarian cancer, including high-grade serous ovarian carcinoma, clear cell carcinoma, and endometrioid carcinoma, have been considered to arise from tissues that do not normally exist in the ovary. Most high-grade serous ovarian carcinomas are thought to arise from the fallopian tube as serous tubal intraepithelial carcinoma (STIC) [25]. Our data show that OCTL14 not only preferentially accumulates in ovarian cancer but also in fallopian tubes *in vivo*, indicating that OCTL14 is able to detect ovarian cancer and its originating cell lineage reliably. Together, these results suggest that the main entry mechanism by which OCTL14 enters cells involves OCTs. To examine the subcellular localization of OCTL14, double staining with OCTL14 and commercially available MitoTracker or LysoTracker Green in cultured ID8 cells and imaging was performed. LysoTracker Green revealed significant co-localization of OCTL14 with lysosomes (76.2%), while MitoTracker Green showed a lack of co-localization of OCTL14 with mitochondria after 30-min incubation (18.7%) (**Fig. 4d,e**). No signal was observed in nuclei. Due to the positive charge of the quaternary anime, OCTL14 is sequestered and retained in lysosomes via lysosomal trapping [26]. In addition, cancer cells are reported to show lower pH in lysosomes compared to normal cells [27], which would favor cellular retention of cations including OCTL14 in cancer tissue. Next, FGS was performed using the optimized dose of OCTL14 in the ovarian cancer model of peritoneal dissemination [28]. The fluorescent images provided precise localization of peritoneal metastatic nodules 6 h post-injection and enabled the surgeon to achieve complete resection of metastatic nodules, including a small nodule measuring < 1 mm in size with no residual tumor (**Fig. 5a, Fig. S11**, **Movie S1**). Images of the resected tumors demonstrate the successful resection of peritoneal disseminations ranging in size from < 1 mm to 5 mm (**Fig. 5a, Fig. S11**). The average number of tumors found using the color image with the NIR image (49.3) was significantly higher than those detected using just the color images (23.7) by experienced surgeons (**Fig. 5b**, $*P < 0.05$), demonstrating the positive clinical impact of the use of OCTL14. Ureteral injury is one of the most frequent intraoperative complications in gynecological surgery [29]. Therefore, dual imaging of tumors with OCTL14 and ureters with a renal clearable zwitterionic NIR fluorophore, ZW800-PEG, was performed [30]. In the 700-nm channel images, we were able to identify variously sized tumors with OCTL14 as expected. In the 800-nm channel images, we could also clearly locate the ureter (**Fig. 5c**). The fluorescence signal from the ureter could be detectable starting from 5 min and lasted up to at least 3 hours after a single bolus injection of ZW800-PEG. Although the SBR for the ureter at 5 min was low compared to its peak SBR at 2.5 h, the fluorescence signals of ureters were sufficiently high to locate ureters during the dual imaging (**Fig. 5d**). Thus, the combination of these two NIR fluorophores is suitable for gynecologic surgery with dual-channel NIR imaging.

Conclusion

A new squaraine fluorophore OCTL14 displays optimal optical and pharmacokinetic profiles for FGS with high TBR and a durable imaging time window in an established preclinical ovarian cancer model. Intravenous administration of OCTL14 as a contrast agent facilitated the accurate localization of small metastatic nodules throughout the abdominal cavity. Delineating the tumors visually by FGS using NIR imaging would provide surgeons an indispensable tool to detect tumors easily and reproducibly (**Fig. 5e**). Moreover, using the renal clearable ZW800-PEG for simultaneous visualization of the ureter, we achieved dual intraoperative imaging for tumors and ureters. We also identified the primary mechanisms of the tumor targetability of OCTL14 in which OCTL14 enters cells *via* OCTs and is retained in the lysosome, achieving rapid and durable intraoperative imaging after a single intravenous injection with high specificity and sensitivity. The potential for the early diagnosis of ovarian cancer warrants further exploration of the squaraine to achieve the positive clinical impact of this approach.

Acknowledgements

We thank Wesley Stiles for manuscript editing. This study was supported by NIH grants NIBIB #R01EB022230 and NHLBI #R01HL143020, and the Creative Materials Discovery Program through the National Research Foundation of Korea (2019M3D1A1078938). SY was supported by a study abroad scholarship from CMI Inc. (Tokyo, Japan). The contents of this paper are solely the responsibility of the authors and do not necessarily reflect the official views of the National Institutes of Health.

Keywords

Ovarian Cancer • Intraoperative Near-infrared Fluorescence Imaging • Squaraine • Organic Cation Transporter • Lysosome

[1] aJ. Ferlay, M. Colombet, I. Soerjomataram, C. Mathers, D. M. Parkin, M. Piñeros, A. Znaor, F. Bray, *Int J Cancer* **2019**, *144*, 1941-1953; bR. D. Cress, Y. S. Chen, C. R. Morris, M. Petersen, G. S. Leiserowitz, *Obstet Gynecol* **2015**, *126*, 491-497.

[2] aA. du Bois, A. Reuss, E. Pujade-Lauraine, P. Harter, I. Ray-Coquard, J. Pfisterer, *Cancer* **2009**, *115*, 1234-1244; bU. A. Matulonis, A. K. Sood, L. Fallowfield, B. E. Howitt, J. Sehouli, B. Y. Karlan, *Nat Rev Dis Primers* **2016**, *2*, 16061; cR. E. Bristow, J. Chang, A. Ziogas, H. Anton-Culver, *Obstet Gynecol* **2013**, *121*, 1226-1234; dS. J. Chang, M. Hodeib, J. Chang, R. E. Bristow, *Gynecol Oncol* **2013**, *130*, 493-498; eA. J. Cortez, P. Tudrej, K. A. Kujawa, K. M. Lisowska, *Cancer Chemother Pharmacol* **2018**, *81*, 17-38.

[3] U. H. Weidle, F. Birzele, G. Kollmorgen, R. Rueger, *Cancer Genomics Proteomics* **2016**, *13*, 407-423.

[4] aS. Gioux, H. S. Choi, J. V. Frangioni, *Mol Imaging* **2010**, *9*, 237-255; bE. A. Owens, S. Lee, J. Choi, M. Henary, H. S. Choi, *Wiley Interdisciplinary Reviews: Nanomedicine and Nanobiotechnology* **2015**, *7*, 828-838; cE. A. Owens, M. Henary, G. El Fakhri, H. S. Choi, *Acc Chem Res* **2016**, *49*, 1731-1740.

[5] T. Nagaya, Y. A. Nakamura, P. L. Choyke, H. Kobayashi, *Front Oncol* **2017**, *7*, 314-314.

[6] aE. De Boer, N. Harlaar, A. Taruttis, W. Nagengast, E. Rosenthal, V. Ntziachristos, G. van Dam, *British Journal of Surgery* **2015**, *102*; bT. Hussain, Q. T. Nguyen, *Adv Drug Deliv Rev* **2014**, *66*, 90-100.

[7] aH. S. Choi, W. Liu, F. Liu, K. Nasr, P. Misra, M. G. Bawendi, J. V. Frangioni, *Nat Nanotechnol* **2010**, *5*, 42-47; bH. S. Choi, K. Nasr, S. Alyabyev, D. Feith, J. H. Lee, S. H. Kim, Y. Ashitate, H. Hyun, G. Patonay, L. Strekowski, M. Henary, J. V. Frangioni, *Angew Chem Int Ed Engl* **2011**, *50*, 6258-6263.

[8] aJ. V. Frangioni, *Curr Opin Chem Biol* **2003**, *7*, 626-634; bE. A. Owens, H. Hyun, T. L. Dost, J. H. Lee, G. Park, D. H. Pham, M. H. Park, H. S. Choi, M. Henary, *J Med Chem* **2016**, *59*, 5311-5323.

[9] aS. Luo, E. Zhang, Y. Su, T. Cheng, C. Shi, *Biomaterials* **2011**, *32*, 7127-7138; bM. Zhao, L. Dong, Z. Liu, S. Yang, W. Wu, J. Lin, *Quant Imaging Med Surg* **2018**, *8*, 151-160; cM. Staderini, A. Megia-Fernandez, K. Dhaliwal, M. Bradley, *Bioorg Med Chem* **2018**, *26*, 2816-2826; dB. P. Joshi, T. D. Wang, *Contrast Media Mol Imaging* **2018**, *2018*, 2015237; eH. Kim, H. S. Choi, S. K. Kim, B. I. Lee, Y. Choi, *Theranostics* **2017**, *7*, 952-961.

[10] Y. Ji, Z. Wang, K. Bao, G. K. Park, H. Kang, S. Hu, E. McDonald, M. S. Kim, S. Kashiwagi, H. S. Choi, *Quant Imaging Med Surg* **2019**, *9*, 1548-1555.

[11] aL. Borsi, E. Balza, M. Bestagno, P. Castellani, B. Carnemolla, A. Biro, A. Leprini, J. Sepulveda, O. Burrone, D. Neri, L. Zardi, *Int J Cancer* **2002**, *102*, 75-85; bM. Carrasco-Triguero, J. H. Yi, R. Dere, Z. J. Qiu, C. Lei, Y. Li, C. Mahood, B. Wang, D. Leipold, K. A. Poon, S. Kaur, *Bioanalysis* **2013**, *5*, 1007-1023.

[12] aK. Kleinmanns, V. Fosse, B. Davidson, E. G. de Jalon, O. Tenstad, L. Bjorge, E. McCormack, *EBioMedicine* **2020**, *56*, 102783; bC. Zhang, X. Ling, Y. Guo, C. Yuan, H. Cheng, X. Ye, R. Ma, Y. Zhang, Y. Li, X. Chang, B. Kong, T. Liu, H. Cui, *Chin J Cancer Res* **2019**, *31*, 673-685.

[13] aM. W. Dewhirst, T. W. Secomb, *Nat Rev Cancer* **2017**, *17*, 738-750; bC. S. Kue, A. Kamkaew, K. Burgess, L. V. Kiew, L. Y. Chung, H. B. Lee, *Med Res Rev* **2016**, *36*, 494-575.

[14] aG. M. van Dam, G. Themelis, L. M. Crane, N. J. Harlaar, R. G. Pleijhuis, W. Kelder, A. Sarantopoulos, J. S. de Jong, H. J. Arts, A. G. van der Zee, J. Bart, P. S. Low, V. Ntziachristos, *Nat Med* **2011**, *17*, 1315-1319; bC. E. Hoogstins, Q. R. Tummers, K. N. Gaarenstroom, C. D. de Kroon, J. B. Trimbos, T. Bosse, V. T. Smit, J. Vuyk, C. J. van de Velde, A. F. Cohen, P. S. Low, J. Burggraaf, A. L. Vahrmeijer, *Clin Cancer Res* **2016**, *22*, 2929-2938; cL. M. Randall, R. M. Wenham, P. S. Low, S. C. Dowdy, J. L. Tanyi, *Gynecol Oncol* **2019**, *155*, 63-68.

[15] I. Veys, F. C. Pop, S. Vankerckhove, R. Barbieux, M. Chintinne, M. Moreau, J. M. Nogaret, D. Larsimont, V. Donckier, P. Bourgeois, G. Liberale, R. Group, D. f. t. C. A. o. F. I. o. t. J. B. Institute, *J Surg Oncol* **2018**, *117*, 228-235.

[16] aQ. R. Tummers, C. E. Hoogstins, A. A. Peters, C. D. de Kroon, J. B. Trimbos, C. J. van de Velde, J. V. Frangioni, A. L. Vahrmeijer, K. N. Gaarenstroom, *PLoS One* **2015**, *10*, e0129766; bH. S. Choi, H. K. Kim, *Nat Biomed Eng* **2020**, *4*, 245-246.

[17] aH. Hyun, H. Wada, K. Bao, J. Gravier, Y. Yadav, M. Laramie, M. Henary, J. V. Frangioni, H. S. Choi, *Angew Chem Int Ed Engl* **2014**, *53*, 10668-10672; bH. Hyun, M. H. Park, E. A. Owens, H. Wada, M. Henary, H. J. Handgraaf, A. L. Vahrmeijer, J. V. Frangioni, H. S. Choi, *Nat Med* **2015**, *21*, 192-197.

[18] K. Ilina, W. M. MacCuaig, M. Laramie, J. N. Jeouty, L. R. McNally, M. Henary, *Bioconjug Chem* **2020**, *31*, 194-213.

[19] Y. Yadav, E. Owens, S. Nomura, T. Fukuda, Y. Baek, S. Kashiwagi, H. S. Choi, M. Henary, *J Med Chem* **2020**, *63*, 9436-9445.

[20] U. Mayerhoffer, M. Gsanger, M. Stolte, B. Fimmel, F. Wurthner, *Chemistry* **2013**, *19*, 218-232.

[21] M. Matsui, H. Mase, J.-Y. Jin, K. Funabiki, T. Yoshida, H. Minoura, *Dyes and Pigments* **2006**, *70*, 48-53.

[22] G. K. Park, J. H. Lee, E. Soriano, M. Choi, K. Bao, W. Katagiri, D. Y. Kim, J. H. Paik, S. H. Yun, J. V. Frangioni, T. E. Clancy, S. Kashiwagi, M. Henary, H. S. Choi, *iScience* **2020**, *23*, 101006.

[23] aM. Roth, A. Obaidat, B. Hagenbuch, *Br J Pharmacol* **2012**, *165*, 1260-1287; bC. Volk, *Wiley Interdisciplinary Reviews: Membrane Transport and Signaling* **2014**, *3*, 1-13; cH. Koepsell, K. Lips, C. Volk, *Pharm Res* **2007**, *24*, 1227-1251.

[24] X. Yang, C. Shi, R. Tong, W. Qian, H. E. Zhau, R. Wang, G. Zhu, J. Cheng, V. W. Yang, T. Cheng, M. Henary, L. Strekowski, L. W. Chung, *Clin Cancer Res* **2010**, *16*, 2833-2844.

[25] A. N. Karnezis, K. R. Cho, C. B. Gilks, C. L. Pearce, D. G. Huntsman, *Nat Rev Cancer* **2017**, *17*, 65-74.

[26] F. Kazmi, T. Hensley, C. Pope, R. S. Funk, G. J. Loewen, D. B. Buckley, A. Parkinson, *Drug Metab Dispos* **2013**, *41*, 897-905.

[27] B. A. Webb, F. M. Aloisio, R. A. Charafeddine, J. Cook, T. Wittmann, D. L. Barber, *Mol Biol Cell* **2021**, *32*, 131-142.

[28] K. F. Roby, C. C. Taylor, J. P. Sweetwood, Y. Cheng, J. L. Pace, O. Tawfik, D. L. Persons, P. G. Smith, P. F. Terranova, *Carcinogenesis* **2000**, *21*, 585-591.

[29] aE. Manoucheri, S. L. Cohen, E. M. Sandberg, A. S. Kibel, J. Einarsson, *Rev Obstet Gynecol* **2012**, *5*, 106-111; bJ. A. Goodno, Jr., T. W. Powers, V. D. Harris, *Am J Obstet Gynecol* **1995**, *172*, 1817-1820; discussion 1820-1812.

[30] C. Yang, H. Wang, S. Yokomizo, M. Hickey, H. Chang, H. Kang, T. Fukuda, M. Y. Song, S. Y. Lee, J. W. Park, K. Bao, H. S. Choi, *Angew Chem Int Ed Engl* **2021**, *60*, 13847-13852.

Entry for the Table of Contents

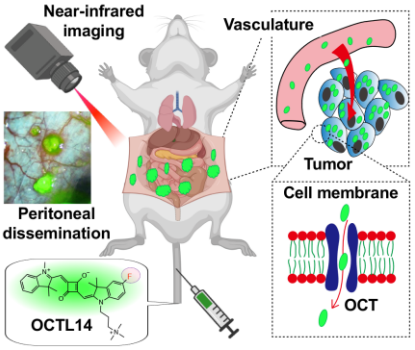

A new squaraine fluorophore OCTL14 displays ultrabright optical properties and optimal pharmacokinetics, allowing high contrast and durable near-infrared imaging for fluorescence-guided surgery of ovarian cancer. The primary mechanisms of the tumor targetability of OCTL14 involve its rapid diffusion across tumor vasculature and cellular uptake *via* organic cation transporters and retention in the lysosome.